

ORIGINAL ARTICLE

Plasmon management in index engineered 2.5D hybrid nanostructures for surface-enhanced Raman scattering

Yi-Fan Huang¹, Chiung-Yi Chen², Li-Chyong Chen², Kuei-Hsien Chen^{2,3} and Surojit Chattopadhyay^{1,4}

Leaky mode resonance (LMR) and optical standing waves (SWs) generated in suitably illuminated vertically aligned supported nanowires (NWs) were demonstrated to enhance the plasmonic electric (E) field behavior of silver nanoparticles (AgNPs) dispersed on the wires. The combination of LMR and SW can significantly enhance the local plasmonic E field around high-density AgNPs. The results of the finite difference time domain (FDTD) calculations were experimentally verified by comparing the surface-enhanced Raman scattering (SERS) sensitivity, which is directly dependent on the E field, in AgNP-coated silicon, germanium and silver NWs. As LMR and SW are functions of the substrate optical index (n , k), an engineering of the indices predicted a (3.88, 0) theoretical value to maximize the plasmonic E -field on the hybrid scaffold at a given AgNP density. These SERS substrates were utilized for the detection of marine toxins, L-BMAA (2-amino-3-(methylamino) propionic acid hydrochloride) and Malachite green, which are used extensively in seafood. AgNP-decorated silicon NWs, whose index (3.88, 0.02) lies close to the theoretically predicted value, exhibit at least pico-molar sensitivity toward those marine toxins. A plasmon management strategy is developed that could assist in lowering the detection level of environmental toxins by SERS. *NPG Asia Materials* (2014) 6, e123; doi:10.1038/am.2014.67; published online 12 September 2014

INTRODUCTION

The involvement of plasmonics¹ in applications such as biosensing² through surface-enhanced Raman scattering (SERS), energy,³ photodetectors⁴ and lasers,⁵ among others, is extensive because surface plasmons can concentrate and manipulate light energy on scales lower than their diffraction limit.⁶ The common goal has generally been to be able to intensify and control the plasmonic electric (E) fields in preferred locations within the material. For example, the so-called 'hot-spots' in SERS, for molecular sensing, are reportedly the regions of extraordinarily intense E field at the junctions of critically close gold (Au) or silver (Ag) nanoparticles (NPs). The interparticle spacing⁷ and fractal-like aggregations⁸ within the metal NPs were observed to be more critical for the E enhancement than the basic material properties or the size of the NPs.

The recent observation of enhanced optical absorption in suitably illuminated semiconductor nanowires (NWs) via leaky mode resonances (LMRs)⁹ opens up the possibility of using LMR for the E -field enhancement of metal NPs. In addition, researchers have observed optical standing waves (SWs) along the length of the NWs when studying optically illuminated vertically aligned NW structures grown on a substrate by finite difference time domain (FDTD) calculations. However, the effect of the SWs or the LMR in modulating the total effective E field has been ignored or addressed inadequately. The fact that Ag- or AuNP-dispersed vertically aligned 1D NW/nanorods¹⁰

supported on a 2D wafer, to be called 2.5D hereafter, are better SERS performers^{11–17} indicates a role for both the LMR and the SWs; however, this role has not yet been reported. Such a study is difficult but immensely useful because the hybrid (metal–semiconductor) nanostructures can be used for a wide range of applications such as SERS,^{16–18} photonics,^{4,5} renewable energy³ and biomedicine.^{19–21} This study addresses whether the newly observed optical effects, LMR and SWs in an NW system, can positively affect the plasmonic E field for photonic applications.

To address this query, detailed FDTD calculations were performed on the 2.5D semiconductor nanostructures decorated with AgNPs that included the effects of (i) LMR in the 1D NWs, (ii) SWs generated in the NWs due to the substrate, (iii) the locations of the AgNPs with respect to the SWs, (iv) optical indices of the NWs and the substrate that will affect both the LMR and the SWs, and (v) the AgNP density.

To validate the theoretical predictions of the plasmon management, we chose SERS as the experimental platform because SERS is fundamentally based on the plasmonic enhancement of the E field,^{22,23} and the technique is evolving as a major tool for inclusion of environmental safety²⁴ in the ultra-sensitive toxic screening of food products.²⁵ Existing high-performance nanostructured SERS substrates are more chanced upon than rationally developed. A fundamental understanding of the plasmon

¹Institute of Biophotonics, National Yang-Ming University, Taipei, Taiwan; ²Center for Condensed Matter Sciences, National Taiwan University, Taipei, Taiwan; ³Institute of Atomic and Molecular Sciences, Academia Sinica, Taipei, Taiwan and ⁴Biophotonics and Molecular Imaging Research Center, National Yang Ming University, Taipei, Taiwan
Correspondence: Professor S Chattopadhyay, Institute of Biophotonics, National Yang-Ming University, No. 155, Section 2, Li-Nong Street, Taipei 112, Taiwan.
E-mail: sur@ym.edu.tw

Received 18 April 2014; revised 5 June 2014; accepted 23 June 2014

management might lead to a design principle, including the architecture and selection of a material for the SERS scaffold that could lower the limit of detection in sensing applications. We have modeled the plasmonics of our 2.5D substrates, AgNP-coated, vertically aligned NW arrays, by FDTD and clarify the role of the five significant factors mentioned above in controlling the E field. The theoretical predictions are then directly corroborated by the experimental SERS observation for screening toxic food additives. Finally, we predict a 2.5D material design by mapping the optical index (n, k) space for the development of a hybrid SERS substrate that would support the highest E field for ultrasensitive detection and possible photonic applications.

EXPERIMENTAL PROCEDURES

Fabrication of the silicon nanowires

The silicon nanowire (SiNW) arrays on 6-inch silicon substrates were fabricated using a top-down type self-masked dry etching process. A high-density electron cyclotron resonance microwave plasma of SiH_4 , CH_4 , H_2 , and Argon (Ar) was used to physico-chemically etch the Si wafers. Typical gas flow ratios of $\text{SiH}_4:\text{CH}_4:\text{Ar}:\text{H}_2 = 0.2:3:5:8$, a microwave power of 1200 W, a substrate temperature of $\sim 200^\circ\text{C}$ and an etching time of 10 h were used.^{26–28}

Ion-beam-sputtering deposition of AgNPs

The plasmonic AgNPs were coated on the SiNWs using the ion-beam sputtering process. The sputtering chamber contained a 2-inch Ag target mounted on a rotating stage, and the SiNW substrates were held ~ 15 cm away from the target. An Ar ion beam (flow rate of 2 sccm), using an Ion Tech, Inc. (Fort Collins, CO, USA) (MPS-3000FC) controller, was incident on the Ag target at 5×10^{-4} Torr pressure at room temperature, and the deposition time was varied from 10 to 40 min to achieve different loadings of the AgNPs on the SiNW surface.

High-resolution scanning electron microscopy

High-resolution scanning electron microscopy (HRSEM) was performed with a JEOL (Tokyo, Japan) FESEM 6700F to characterize the morphology, particle size, and loading density of the NWs and the AgNPs.

Surface-enhanced Raman spectroscopy

Raman spectra were obtained using a commercial Jobin Yvon LabRAM HR800 (HORIBA Ltd., Kyoto, Japan) equipped with a $\times 100$ microscope objective and a liquid-nitrogen-cooled CCD detector using a back-scattering geometry. An excitation laser wavelength of 633 nm, a power of 0.6 mW and a focused laser beam spot size of $\sim 2 \mu\text{m}$ (diameter) were used. All single accumulation Raman spectra were acquired with an acquisition time of 20 s. The spectral resolution was 0.6 cm^{-1} .

The marine toxic chemicals, used as analytes, for the SERS experiments were Malachite green ($[\text{C}_6\text{H}_5\text{C}(\text{C}_6\text{H}_4\text{N}(\text{CH}_3)_2)_2\text{Cl}]$, MG, Sigma-Aldrich, St Louis, MO, USA) and L-BMAA (2-amino-3-(methylamino) propionic acid hydrochloride, Sigma-Aldrich). While MG is used as a fungicide in aquaculture, L-BMAA, which is found in shark fins and cycads, is an environmental factor in neurodegenerative diseases. BMAA present in cycads is bio-magnified upon consumption in flying foxes from Guam, where a sizable proportion of the population suffers from neurological disorders attributed to consuming these flying foxes. Different concentrations of MG (10^{-3} to 10^{-12} M) and L-BMAA (10^{-6} to 10^{-15} M) were prepared by serial dilution in deionized water. An aqueous solution of these analytes, $1 \mu\text{l}$ in volume with controlled concentrations, was then dispersed by drop coating onto the SERS substrates (AgNP coated and uncoated NWs of Si, Ge). The substrates were dried in air, and Raman spectroscopy (RS) was performed on them. The substrate area covered by the analyte droplet was $\sim 4 \text{ mm}^2$.

FDTD simulation

3D numerical simulations using the FDTD method (FDTD solutions, Version 7, Lumerical Solutions Inc., Vancouver, BC, Canada) (<http://www.lumerical.com>)

were performed to determine the spatial distribution of the near field plasmonic E field for various substrate configurations and AgNP loading densities. The simulation parameters included a time step of 0.001 fs, a mesh size of 1 nm (in all three directions, dx , dy and dz), and a background index of 1.0 (air), unless otherwise mentioned. The known indexes of Ag and various semiconductor substrates (such as Si, GaAs and Ge) were acquired from Palik.²⁹ Perfectly matched layer boundary conditions were applied along the x -, y -, and z -boundaries of the unit cell. The accuracy of the results was confirmed through convergence tests. E -field mapping of the AgNPs distribution for various substrate configurations and materials was performed with a horizontal (X) \vec{E} polarization of the 633 nm excitation under normal incidence. A schematic illustration of the FDTD model and additional simulation layout setting details is presented in Supplementary Figure S1. Far-field optical simulations of the as-grown SiNW by FDTD have been reported elsewhere.³⁰

RESULTS AND DISCUSSION

Keys to plasmon management in 2.5D nanostructures by FDTD

The key elements for effective plasmon management in the 2.5D nanostructures through the extensive FDTD simulations (model, Supplementary Figure S1) are presented in Figure 1. First, we demonstrate why the NW or NR scaffold is preferred for AgNP dispersion for SERS applications. The obvious reason is the ability of the NW to load more AgNPs due to the large available surface area compared with a 2D substrate. The less obvious reason is the recent observation of enhanced optical absorption, through LMR, in an NW with a select diameter for a selected energy of illumination. We observed LMR in the free-standing SiNW (~ 100 nm diameter, $\lambda = 633$ nm excitation) (Figure 1a). Although higher-order LMR modes are present, such as HE_{12} , it is the HE_{11} mode³¹ (at 576 nm) that couples with the plasmon and alters the E field over the NW surface. The contribution of this HE_{11} mode to the E field under different wavelength excitations is demonstrated in Supplementary Figure S2 and is significant even at 633 nm. The E field resulting from these LMRs can also be modulated by the optical indices (n, k) of the material.⁹ Once the size of the SiNWs and the excitation wavelength are fixed experimentally, a variation of (n, k) will result in regions of stronger $|E|^2_{\text{max}}$ values, as we will observe later.

Next, when a Si substrate is added to the SiNW (bottom panel, Figure 1b), completing the 2.5D structure, classical wave-guiding principles cause the SWs along the length of the SiNW, revealing clear node and anti-node features. The SWs would not be present if the NWs are lying down on the substrate. The support, depending on its optical indices (n, k) (real and imaginary parts of the complex refractive index $N = n + i k$), will reflect the incident light waves to create the SWs along the length of the NW. The number of SW modes ($M = 1, 2, 3, \dots$) follows the rule $L = (2M - 1)\lambda/4$, where L is the length of the SiNW. We have confirmed the existence of the SWs by varying the length of the NWs to observe higher modes ($M = 2, 3, 4, \dots$) in longer NWs (see Supplementary Figure S3). For the real case, where $L = 1300$ nm and $\lambda = 633$ nm was used, $M = 4$, and the 4th harmonic of the SW was observed (bottom panel, Figure 1b). These SWs provide a background for the LMR absorption spectrum and a modulation of the total E field (Supplementary Figures S2–I).

The formation of the SW resulting from the interference between the incident and reflected wavetrains is illustrated in Supplementary Figure S4. The effect of the SWs on the E -field distribution in such vertically aligned NWs used for SERS in the backscattering geometry (light propagation vector K and the E field is along and perpendicular to the NW axis) has also been tested under different K and E polarizations (see Supplementary Figure S5). Clearly, the effect of the

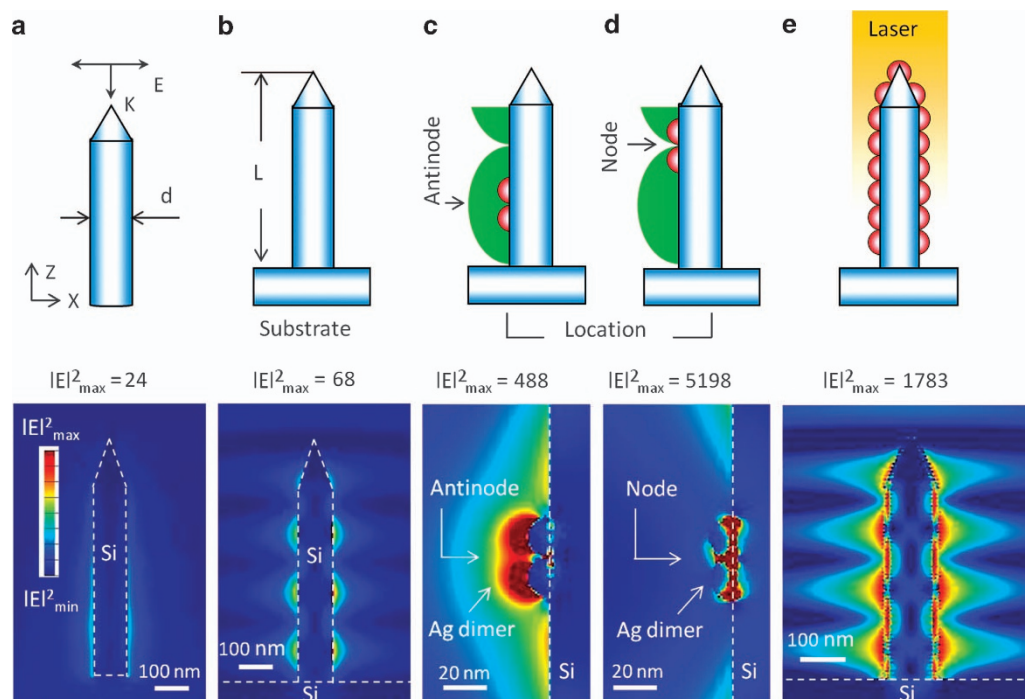


Figure 1 Plasmon management in vertically aligned 2.5D SiNWs, with diameters of 100 nm and lengths of 1300 nm, with AgNPs. (Top panel) Schematic diagrams of vertically aligned (a) free-standing and (b) supported SiNW. Supported SiNW with an Ag dimer (dia. ~ 20 nm, gap = 1 nm) at the (c) anti-node and (d) node locations of the resulting standing waves (SWs) along the length (L , along Z) of the SiNW. (e) Schematic of a supported SiNW with high-density AgNPs under real SERS experimental conditions. (Bottom panel) Corresponding FDTD electric (E)-field mapping images show (a) LMRs in a free-standing SiNW and (b) SW-modulated LMR in a supported SiNW; total E field, under the sum effect of SW and LMR, around the Ag dimer when placed at (c) the anti-node and (d) the node locations of the SW. (e) Plasmonic E -field mapping image for a supported SiNW with high-density AgNPs showing LMR, SW, and AgNP surface plasmons. K represents the propagation direction of the incident 633-nm light wave. The maximum values of $|E|^2$ ($|E|_{\max}^2$) calculated by FDTD are shown for each E -field mapping image.

SWs, represented by the $|E|_{\max}^2$ value, is highest with the back-scattering geometry. Conclusively, the effect of the SW and the LMR on the total E -field distribution is significant, with or without the AgNPs, and can be used beneficially for the SERS study.

With the E field over the scaffold, including the effects of LMR and SWs, being established, we can now introduce the plasmonic AgNPs (Figures 1c and d) into this system. SW is critical for the surface plasmon management, as we observe that the Ag dimer exhibits different $|E|_{\max}^2$ strengths when placed at the anti-node (Figure 1c) and the node locations (Figure 1d) of the SW. Taking all these effects into consideration, a real supported SiNW with high-density AgNPs is modeled for the E -field (Figure 1e) to indicate its relative performance index. A stronger $|E|_{\max}^2$ value would imply a stronger SERS signal and hence a lower limit of detection. The materials, dimensions and excitation selected for the simulation are used to mimic the real SERS experimental conditions to allow verification of these predictions. Overall, Figure 1 conveys a total strategy for the plasmon management.

Morphology and architecture of the 2.5D SERS substrate

For real experiments, we fabricated large-scale arrays of vertically aligned pencil-like NWs^{26–28} on a support decorated with AgNPs as our 2.5D SERS substrate (Figures 2a–h); this design is also shown schematically in Figure 2i. The NWS had cylindrical wire-like bodies and tapered apices, giving the pencil-like appearance (Supplementary Figure S1b). Using plasma processing, we could not fabricate the AgNWs required for the comparative study. Hence, we approximated an SiNW with an optically thick and conformal Ag coating

(deposition time of ≥ 40 min) to be equivalent to an AgNW. For the current experiments and simulations, a length of ~ 1300 nm and a diameter d of ~ 100 were selected for the NWs to load a high density of AgNPs and to support enough SW modes ($M = 4$). An NW longer than 1300 nm would be difficult to coat with AgNPs using the sputtering process. Moreover, with the absorption depth of 633 nm light in silicon being $\sim 1 \mu\text{m}$, Raman signals originating deeper would not be detected. A shorter NW, however, would not support enough SW modes (see Supplementary Figure S3b and c) to demonstrate its effect.

Subsequently, the ion-beam-sputtering deposition process¹¹ was adopted for the deposition of AgNPs on the NW surface. The number density of the AgNPs, and hence the average interparticle distances, could be easily controlled as a function of the sputtering time (t). Figures 2e–h present SEM images of individual SiNWs without and with AgNPs (~ 5 –25 nm). Up to 20 min of sputtering, AgNPs were obtained, beyond which, at ~ 40 min, a thick Ag film with embedded AgNPs was obtained (Figure 2i).

SERS measurement on 2.5D SiNW with AgNPs

To evaluate the SERS activity of the differently AgNP-coated SiNW SERS substrates, MG and L-BMAA were used as analytes. These two molecules are important because they constitute the two most widely used toxic substances in seafood consumed worldwide.^{32,33} Figures 3a and b show the SERS signals of 1 mM of MG (Figure 3a) and 1 μM of L-BMAA (Figure 3b) collected from AgNP-coated SiNW substrates with $t = 0$ –40 min. The characteristic spectral features of MG and L-BMAA can be clearly identified on the SERS data ($t = 10$ –40 min) compared with the conventional Raman spectroscopy data ($t = 0$

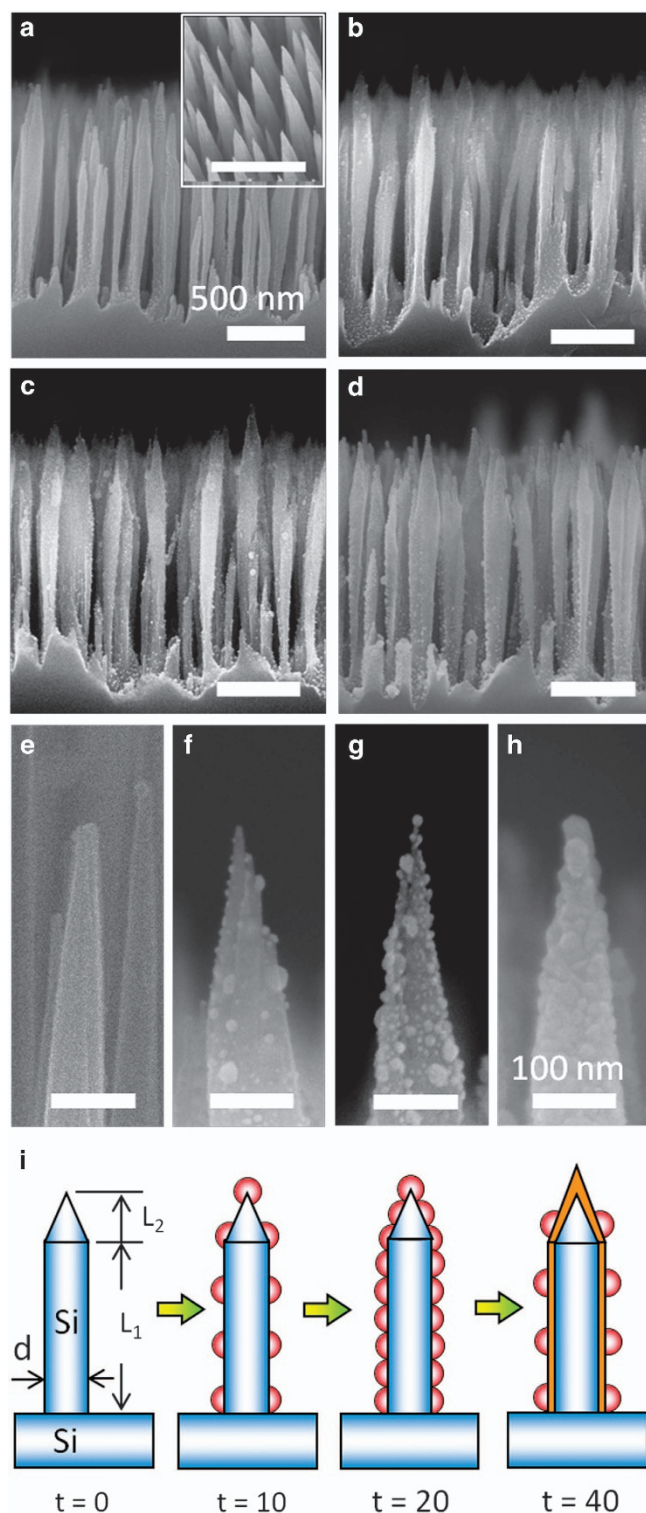


Figure 2 SEM images of the as-grown and AgNP-coated 2.5D pencil-like SiNW. Cross-sectional HRSEM images of SiNW with Ag deposition times of $t =$ (a) 0, (b) 10, (c) 20 and (d) 40 min, respectively. The inset in (a) presents a tilted top view SEM image of the SiNWs. Cross-sectional HRSEM images of the apex of individual SiNW with Ag deposition times of $t =$ (e) 0, (f) 10, (g) 20 and (h) 40 min, respectively. (i) A schematic description of the SiNW, height L_1 , tapered height L_2 , diameter d , with increasing density of self-assembled AgNP (red spheres) as a function of Ag deposition time. At $t = 40$ min, a continuous Ag film with AgNPs results. The scale bar is 500 nm in (a–d) and 100 nm in (e–h).

min). The SERS spectral intensity increases to a maximum for the $t = 20$ min substrate but then decreases for longer values of t .

Having optimized the density of the AgNPs at $t = 20$ min for the maximum SERS intensity, we then investigated the concentration-dependent SERS spectra of MG and L-BMAA to understand the sensitivity of the optimized substrate. Figures 3c and d show the MG and L-BMAA fingerprint SERS bands, respectively, decreasing in intensity with decreasing concentration ($1 \text{ mM} - 1 \text{ pM}$ for MG and $1 \mu\text{M} - 1 \text{ fM}$ for L-BMAA). The characteristic bands of MG and L-BMAA were detectable up to 1×10^{-12} and $1 \times 10^{-15} \text{ M}$, respectively, on the optimized substrate. Hence, the limit of detection is at least 1 pM . Although there are some reports of MG detection via SERS,³⁴ reports on L-BMAA detection in the pico-molar concentrations did not appear in our search. For an estimation of the substrate sensitivity, we investigated the strength of the 1176 cm^{-1} band for MG, which is assigned to the in-plane vibrations of ring C–H, and the 1585 cm^{-1} band for L-BMAA as a function of their respective concentrations. Figures 3e and f reveal the linear variation of the intensity of the signature bands for MG and L-BMAA, respectively. The slope of this line yields the sensitivity of the optimized SERS substrate toward MG and L-BMAA detection over the studied range of concentrations. The reproducibility of the optimized SERS substrate³⁵ can be quantified by obtaining the relative standard deviation ($\text{RSD} = \text{s.d.}/\text{mean}$) from repeated measurements on the same substrate (see Supplementary Figure S6). However, due to the poor adsorption of L-BMAA on the AgNPs, there were significant spectral reproducibility problems at lower analyte concentrations. This issue might be detrimental to quantify the sensitivity of the substrate. Hence, we also used Rhodamine 6G, a common Raman dye, to estimate the sensitivity of the substrate (see Supplementary Figure S7).

To explain the experimental results in Figure 3, it is necessary to consider the effect of AgNP density in our calculations. We have modeled the AgNP distribution (Figure 4) resembling Figure 2 as closely as possible. NWs with no AgNPs ($t = 0$), few AgNPs ($t = 10$ min), maximum AgNPs ($t = 20$ min) and few AgNPs on a Ag thin film ($t = 40$ min) are schematically described for an FDTD simulation in Figures 4a–d, respectively. The corresponding E -field mapping images, for $t = 0, 10, 20, 40$ and 100 min, are presented in the right-hand side panels for SiNW (Column II, Figure 4), GeNW (Column III, Figure 4), GaAsNW (Column IV, Figure 4) and AgNWs (Column V, Figure 4), respectively. The E -field distributions are observed to be riding the NWs in all of these cases with varying intensities, being the strongest for SiNW and the weakest for GeNW, along the Z axes. For each NW case, the E field is the weakest for the $t = 0$ case (Figure 4a). The E -field value (represented by $|E|_{\text{max}}^2$) peaks near $t \sim 20$ min for the SiNW case and near $t = 40$ min for the Ge and Ag NW cases. The line scan profiles of the FDTD results for the $t = 10$ and 40 min cases contain fewer but stronger and frequent but weaker E -field spikes, respectively (Supplementary Figure S8). This finding indicated a stronger SERS signal from the $t = 10$ min sample. However, the surface coverage of the E -field over the entire length of the NW was better for the $t = 40$ min case and indicated better reproducibility of the measurements quantified by the RSD. This phenomenon was also observed experimentally when we compared Supplementary Figure S9a with e and b with f.

Optical index (n , k) engineering for plasmon management

Figure 4 clearly demonstrates that, irrespective of the AgNP density, the E -field distributions on different NWs are different. This finding appears to be an optical index artifact because both LMR and SWs

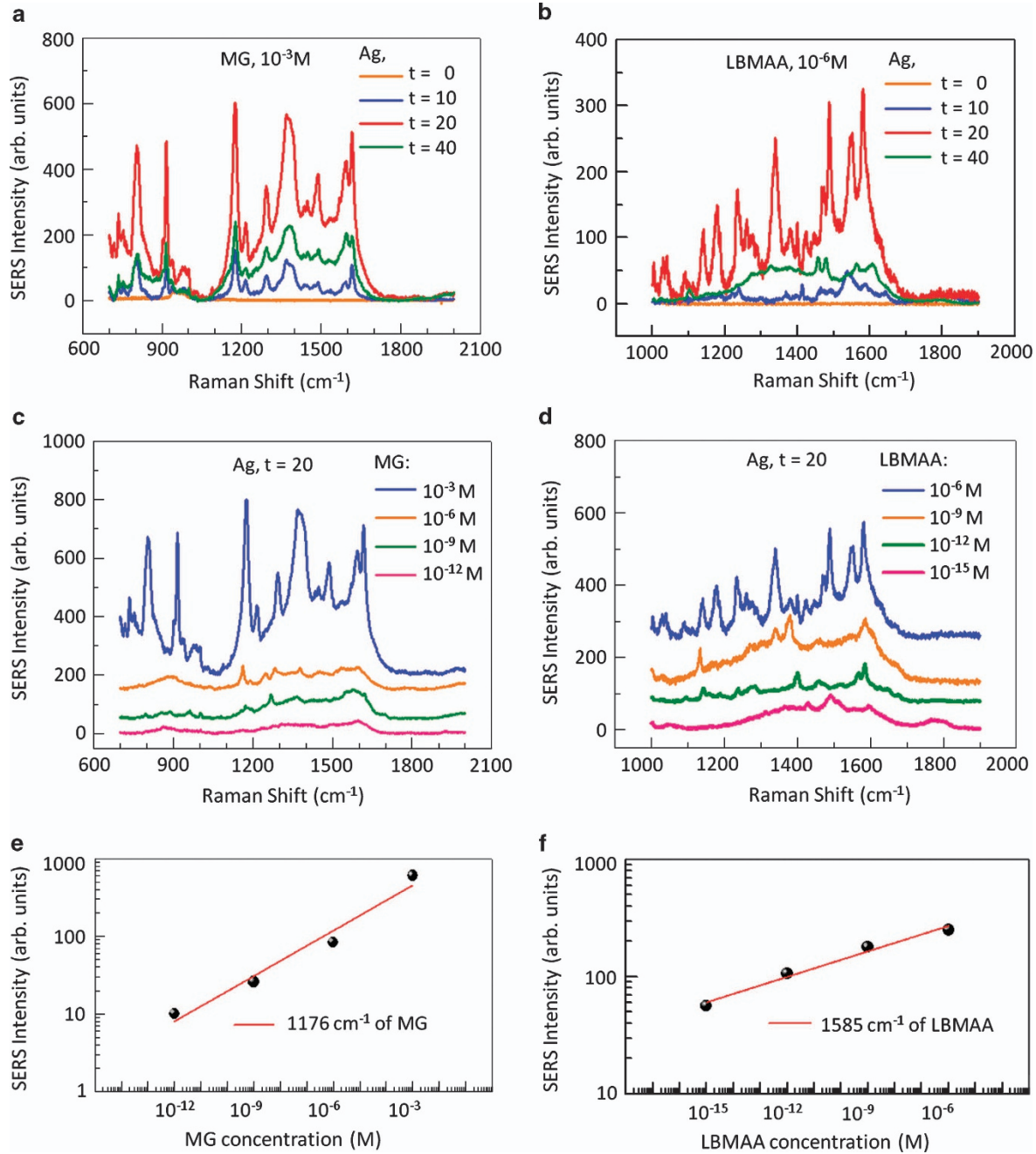


Figure 3 SERS data of MG and L-BMAA on the AgNP-coated SiNW. SERS data of marine toxic chemicals, MG and L-BMAA on Ag-coated SiNW substrates. SERS spectra of (a) 1 mM of MG and (b) 1 μ M of L-BMAA on SiNWs coated with Ag for $t = 0, 10, 20$ and 40 min. SERS data for different concentrations of (c) MG (1 mM–1 μ M) and (d) L-BMAA (1 μ M–1 fM) on $t = 20$ min Ag-coated SiNWs. Variation of the (e) 1176 cm^{-1} Raman line intensity of MG and (f) 1585 cm^{-1} Raman line intensity of L-BMAA as a function of their respective concentrations (as in c and d, respectively). The line joining the data points in (e) and (f) is a linear fit to the data with an R^2 -value of (e) 0.97 and (f) 0.98.

have a direct dependence on the optical indices n and k of the material. It is now imperative to study SW and LMR in materials with different optical indices to arrive at the best-performing hybrid with AgNP.

First, we show four simple models for FDTD simulation: (i) SiNW, (ii) GeNW, (iii) pure AgNW, all with AgNPs ($t = 10$ min), and another (iv) SiNW with AgNPs ($t = 40$ min), as schematically illustrated in Figure 5a. Figure 5b shows the $|E|^2_{\text{max}}$ obtained from the simulation results in Figure 4 for the respective NWs. Clearly,

among the hybrid substrates, the AgNPs@SiNWs (blue) exhibits the highest $|E|^2_{\text{max}}$ value (Figure 5b). The AgNPs@GeNWs (green) exhibits the lowest $|E|^2_{\text{max}}$ value. Because the AgNPs@AgNWs (with $t = 10$ min, data colored red, Figure 5b) exhibit a similar $|E|^2_{\text{max}}$ value as the AgNPs@SiNWs (with $t = 40$ min, data colored orange, Figure 5b), they are considered equivalent. This theoretical equivalence of a $t = 40$ min coated SiNW and a $t = 10$ min coated pure AgNW will be used for our experimental verification because we did not have pure AgNW samples.

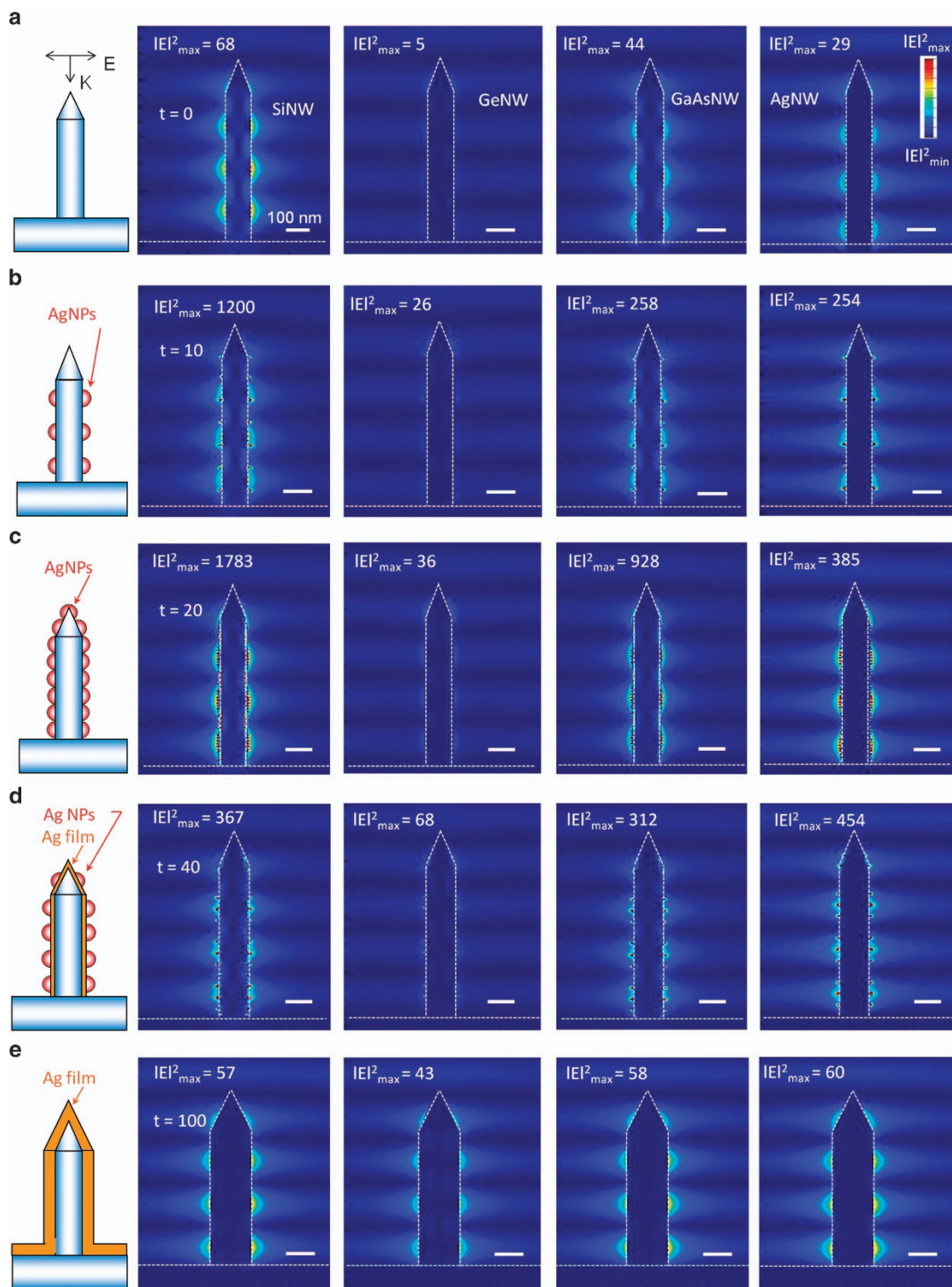


Figure 4 E-field mapping images on AgNP-coated NWs by FDTD. Schematic of a 2.5D NW with Ag coating times of (a) $t=0$, (b) $t=10$, (c) $t=20$, (d) $t=40$ and (e) $t=100$ min. Corresponding (for each t) E-field mapping images for (Column II) SiNW, (Column III) GeNW, (Column IV) GaAsNW and (Column V) AgNW. The calculated value of $|E|^2_{\max}$ is shown in each case. The E-field scale bar is shown in inset (a). Same scale bar of 100 nm in (a-e).

For experimental verification of the FDTD results (Figure 5b), we performed real SERS measurements (Figure 5c) using MG as an analyte on the fabricated SERS substrates. At higher concentrations, we can clearly see that AgNPs@SiNWs exhibits the highest

SERS intensity, and AgNPs@GeNWs exhibits the lowest SERS intensity (top, Figure 5c). At lower MG concentrations, the SERS intensity on AgNPs@GeNWs was negligible, whereas the other two samples exhibited weak but clear spectral features (bottom,

Figure 5c). Comprehensive SERS data are presented in Supplementary Figure S9.

The average SERS signal intensity of the 1176 cm^{-1} band of MG, with two concentrations on those three substrates (see Supplementary Figure S9), is shown in Figure 5d. These experimental data clearly

match the FDTD predictions shown in Figure 5b. AgNPs@GeNWs, where Ge has a high value of k (0.83),²⁹ were inefficient SERS substrates that inhibited the formation of the SW and could not support a strong plasmon field on the dispersed AgNPs (Column III, Figure 4). In addition, the LMR in the GeNWs, $d=100\text{ nm}$, red shifted to 720 nm , which is off-resonance under 633 nm excitation, had weak HE_{11} (see Supplementary Figure S10).

Because the plasma etching process adopted here for the NW fabrication would lead to small variations in the morphology and size of the NWs, there might be a concern that the differences in the $|E|^2_{\text{max}}$ value (Figure 5b) or the SERS intensity (Figure 5d) could be due to such variations. In fact, the experimental GeNW diameters are not 100 nm but $\sim 250\text{ nm}$ (see Supplementary Figure S11). However, the simulations performed on different morphologies and sizes of GeNWs (Supplementary Figure S11) indicate that the variations in the $|E|^2_{\text{max}}$ values are insignificant compared with the differences observed theoretically and experimentally vis-à-vis SiNW or AgNWs (Figure 5). Hence, the results presented in Figure 5 are clearly an artifact of the material (n and k) and the optical effects therein and are not due to small variations in the morphology or sizes normally associated with a controlled growth process. Among the materials considered experimentally, Figure 5 establishes a consistent support for the FDTD prediction that AgNP@SiNWs exhibit better E field. However, is the Ag-Si system the best in the hybrid class?

An answer to our question is provided theoretically by the plasmonic description of different hybrid SERS active substrates shown in Figure 6. FDTD simulations were performed for the E -field distribution in AgNP (varied density)-decorated 2.5D NWs of materials with different n and k values, namely Si, GaAs, Ge, and pure Ag. In Figure 6a, we show FDTD model schematics of individual NWs with different Ag coating times ranging from $t=0$ to 100 min to achieve different AgNP loading densities. In the absence of pure AgNW (for experimental verification), we will assume an equivalent in an SiNW with Ag coating time greater than 40 min (case v, Figure 6a).

With the morphology explained in Figure 6a, we calculated the variation of the $|E|^2_{\text{max}}$ values in high- n and low- k (Si, $N=3.88+i0.02$), high- n and high- k (GaAs, $N=3.85+i0.19$, and Ge, $N=5.47+i0.83$) and pure metal (Ag, $N=0.13+i3.99$) at a wavelength of

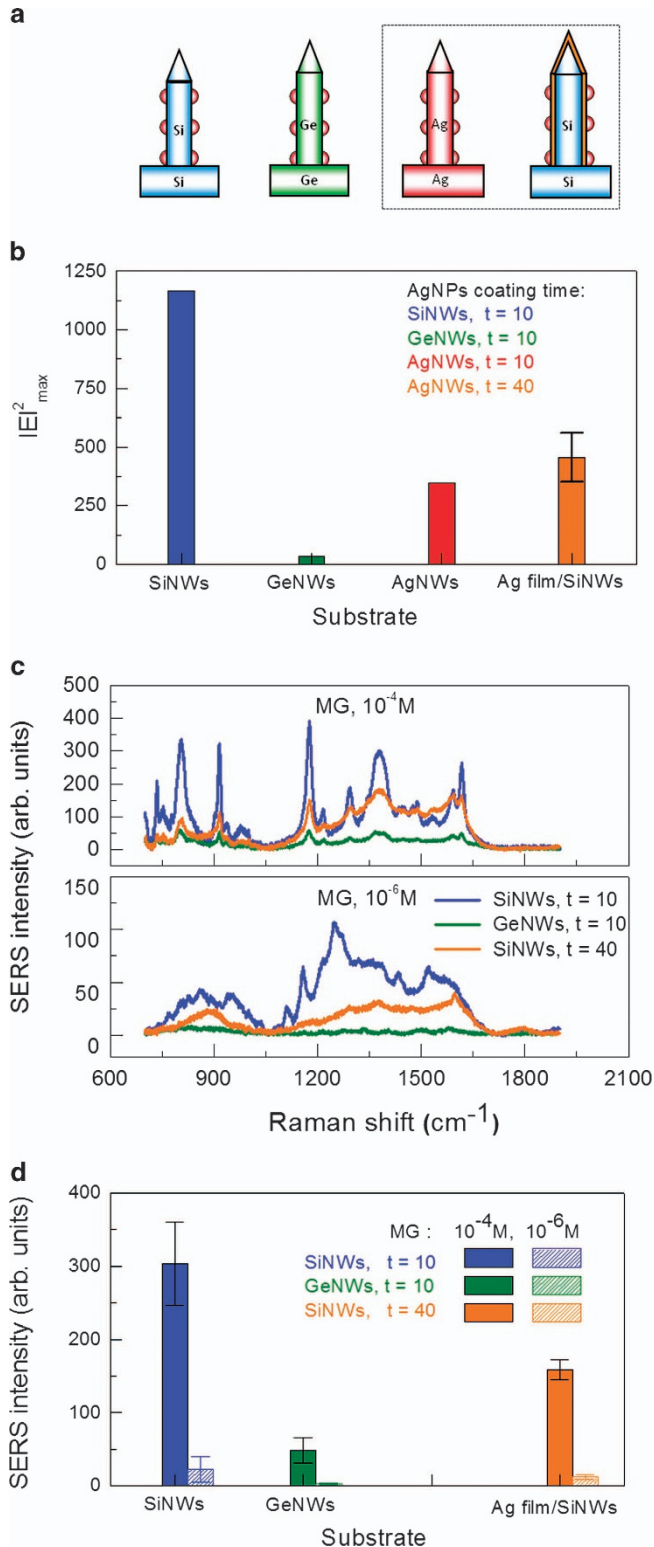


Figure 5 FDTD prediction and experimental SERS corroboration data. (a) Left to right: schematic diagram of AgNP decorated nanowire structures of Si, Ge, pure Ag, and Ag film-coated SiNW. (b) Maximum $|E|^2_{\text{max}}$ values, determined by FDTD, in supported nanostructures of SiNW (Blue), GeNWs (Green), and pure AgNWs (Red) containing the same density of AgNPs obtained with a $t=10\text{ min}$ coating on the SiNW. Because pure AgNWs (third from left in (a)) were not available for experimental verification, we assumed that pure AgNWs are optically equivalent to a thick Ag ($t=40\text{ min}$)-coated SiNW (extreme right in (a)). This assumption is acceptable as the calculated values of maximum $|E|^2_{\text{max}}$ (in (b)) for the nanostructures shown in the box (in (a)) are similar. The error bar in (b) (extreme right) indicates the maximum spread in $|E|^2_{\text{max}}$ for the Ag film-coated SiNW with low (as in Si, Ge, and pure Ag) and high densities (AgNP touching each other) of AgNPs. The $|E|^2_{\text{max}}$ values in SiNWs, GeNWs, and the pure AgNWs are theoretically calculated constants without error bars. (c) Experimental SERS spectra of MG dispersed on real substrates (except for that of pure AgNW (Red), which is theoretical) at concentrations of (top) 10^{-4} M and (bottom) 10^{-6} M . The same color code for the substrate and SERS spectra was maintained in (a–c). (d) The SERS intensity distribution (with error bars) is displayed as a bar chart with data acquired from Supplementary Figure S9 at both analyte concentrations from the real substrates only. All the calculations were performed in air using 633 nm laser irradiation mimicking real experimental conditions.

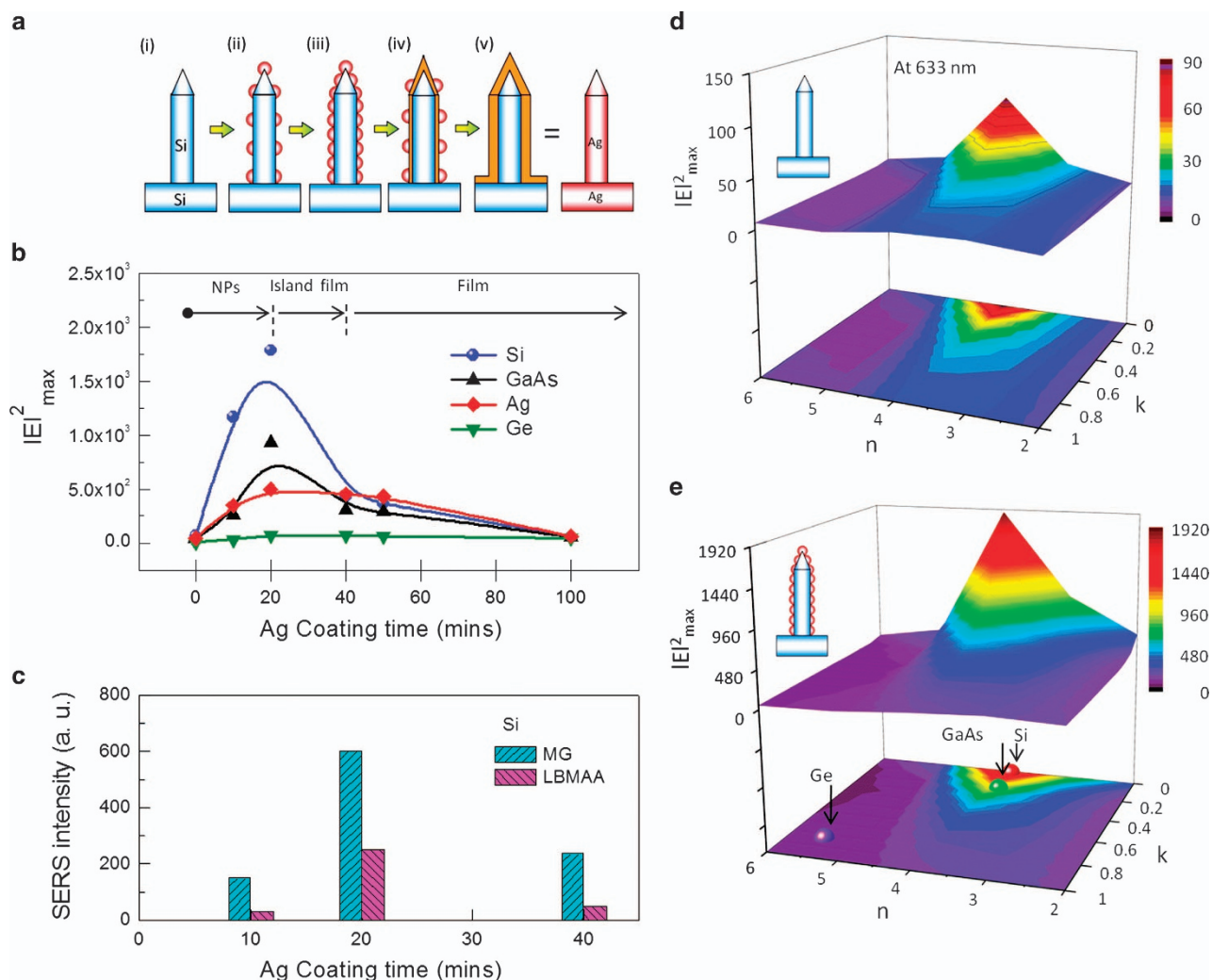


Figure 6 Plasmonic E -field mapping on hybrid substrates by FDTD. (a) Schematic of SiNWs with Ag coating times of $t = (i) 0, (ii) 10, (iii) 20$ (optimized density), $(iv) 40$ and $(v) 100$ min. The schematics are simplified approximations of real SEM images (Figure 2). (b) The variation of $|E|^2_{\max}$ as a function of t on Si, GaAs, Ag, and Ge NW substrates (assuming the same AgNP distribution at each t). The horizontal arrows indicate the metal morphology at different coating times. The line connecting the data points is a guide to the eye only. (c) The variation of selected SERS bands of MG and L-BMAA on AgNP@SiNWs as a function of t . A 3D plot (top) and 2D projection (bottom) of $|E|^2_{\max}$ as a function of material optical indices (n, k) for a vertically aligned NW on a support (d) without the AgNPs and (e) with the highest density of AgNP. Some real materials, such as Si, GaAs and Ge, matching the n, k values were identified in (e).

633 nm (Figure 6b).²⁹ The various NW substrates, with varied n and k values, revealed similar $|E|^2_{\max}$ profiles as a function of t , albeit with variable strengths (Figure 6b). The $|E|^2_{\max}$ data, as a function of different Ag coating times t ($= 0-100$ min), on Si, Ge, GaAs and Ag NW substrates are presented in Figure 4. The E -field profile (Figure 6b) predicts well not only the experimental SERS observed here on MG and L-BMAA (Figure 6c) but also other reports on hybrid-carbon nanotube-based substrates^{36,37} and metal-silica hybrid nanorods, showing improved performance compared with pure silver NRs.³⁸

To predict the best hybrid substrate with the given geometry (Figure 6a (iii)) for SERS application, we systematically calculated $|E|^2_{\max}$ by varying n and k independently in our simulations. The values of the maximum E field were determined from the sidewalls of individual uncoated 2.5D NWs and AgNP@NWs as a function of each n and k combination to produce a three-dimensional plot, as depicted in Figures 6d and e. The real part of the refractive index was varied from $n = 2$ to 6, and the imaginary part was varied from $k = 0$

to 1. The E field has a 3D profile peaking near $n = 4$ and $k = 0$, decaying on both sides of the peak. It is clear that the n and k values significantly affect the 3D E -field profile. This feature is common for both the supported NW architecture without (Figure 6d) and with (Figure 6e) the AgNPs. The magnitude of $|E|^2_{\max}$, however, is higher for the architecture with the AgNPs (scale bar, Figure 6e). The result presented in Figure 6e is not a simple addition of Figure 6d and the plasmonic E -field of the AgNPs. Such high $|E|^2_{\max}$ values could not be obtained without the participation of the SW and the LMR. To demonstrate this point, we simulated an AgNP dimer in air and on a bulk Si wafer, which would not support SW or LMR, under the same configuration used for the NW (see Supplementary Figure S12). The $|E|^2_{\max}$ value, without the SW and the LMR, is far less than the value observed with the SW and the LMR present in a vertically aligned 2.5D NW system.

First, we discuss the effect of non-absorbing substrates ($k = 0$, with varying n value). We observe that initially the $|E|^2_{\max}$ value increases significantly when n increases from 2 to 4, but subsequently decreases

when n increases from 4 to 6. The initial increase in $|E|_{\max}^2$ ($n=2-4$) is correlated with the substrate's reflectivity, which increases with n at normal incidence from the air to the substrate. A higher substrate reflectivity will lead to a stronger SW amplitude along the NW surface, for example, the SiNW (Figure 4a). We have discussed, in Figure 1, that the SWs can improve the E field on the AgNPs at the nodal locations. However, as n increases above 4, the amplitude of the SW-induced $|E|_{\max}^2$ decreases, as calculated by FDTD.

Next, we discuss the effect of optically absorbing substrates ($n=4$, and increasing k). For a fixed $n=4$, the $|E|_{\max}^2$ value rapidly decreases when k increases from 0 to 1. We believe that this finding is attributed to the increase in light absorption in the substrate as k increases, resulting in less optical coupling with the AgNPs for plasmon generation, and at sufficiently high k values, such as for Ge ($k=0.83$), only insignificantly weak SWs and LMR are present along the 2.5D nanostructures. This effect is confirmed by comparing the case of Si ($n=3.88$, $k=0.02$) (Column II, Figure 4) and GaAs ($n=3.85$, $k=0.19$) (Column IV, Figure 4), which have similar n values but different k values. This finding explains the comparatively higher $|E|_{\max}^2$ value in SiNW than that in GaAs NW (Figure 6e).

Finally, we remind the readers that the results presented above must be considered under some general assumptions. First, we assumed perfectly aligned structures and the same AgNP sizes (no distribution) for the FDTD modeling. Experimentally, however, deviations will occur, including clustering of the AgNPs and variations in sizes, which might lead to broad band absorption and improved SERS performance.³⁹ Moderate size variations or agglomerations may cause extraordinary local fields (see Supplementary Figure S13), and hence the current assumption of a uniform distribution of AgNPs would underestimate the actual E field available in these substrates. For calculation purposes, a uniform distribution is easier to model and rationalize than a definition-less random one. Second, we did not assume any change in the optical constant of the metal NPs as a function of size, shape or dielectric environment.^{40,41} Different dielectric media may cause surface plasmon resonance to shift to longer wavelengths or exhibit other resonance modes, such as Fano resonance.⁴² However, in this work, we are only using a single wavelength (633 nm) for real SERS measurements. Tilted nanostructures or 'kissing nanowires'⁴³ and double resonance⁴⁴ did not participate in this discussion. Third, in this work, we only considered single nanostructures for the FDTD simulations because the inter-SiNW distance is >100 nm, as shown in Figure 2. Interwire optical coupling was not considered.⁴⁵ If the individual plasmonic nanostructures, pure metallic or metal-hybrid, come closer than the range (~ 30 nm) of the plasmonic E field, extremely intense local electromagnetic fields can be generated.⁴⁶ In contrast to the localized surface plasmons studied here, for pure metallic NWs, propagating surface plasmons with a guided character can also result in high-sensitivity bio-sensing.⁴⁷ Furthermore, we are only using the classical electromagnetic theory for the calculation and interpretation of results; quantum mechanical effects or chemical enhancement effects have not been considered.^{48,49} However, under a uniform basis and assumptions, the main outcome and the trends of the results would remain unaffected.

CONCLUSIONS

We have presented a plasmon management strategy in vertically aligned 2.5D hybrid NW-AgNP SERS substrates utilizing the effects of LMR and optical SWs observed in them. The plasmonic E field around the high-density AgNPs becomes enhanced in the presence of

the combined effect of LMR and SW. While the LMR ensures higher optical absorption, the SWs provide a modulation of the E field, which is strongest at the node locations of the SWs. Optical index engineering of the scaffold material maximizes the total E field theoretically for a material with $n=3.88$ and $k=0$ at 633 nm and provides key design approaches to help fabricate sensitive hybrid SERS substrates. A vertically aligned 2.5D SiNW ($n=3.88$, $k=0.02$)–AgNP system was experimentally shown to perform similar to the best SERS substrate, among those compared, for the detection of marine toxins, MG and L-BMAA, with at least picomolar levels of SERS sensitivity to support the theoretical prediction.

ACKNOWLEDGEMENTS

This study was supported by the National Science Council, Taiwan, under Grant Nos. NSC 101-2112-M-010-003-MY3 and NSC-101-2120-M-001-010 and the ATU plan of the Ministry of Education, Taiwan. Additional support from the Biophotonics and Molecular Imaging Research Center (BMIRC), National Yang Ming University is also gratefully acknowledged.

- Anker, J. N., Hall, W. P., Lyandres, O., Shah, N. C., Zhao, J. & Van Duyne, R. P. Biosensing with plasmonic nanosensors. *Nat. Mater.* **7**, 442–453 (2008).
- Brolo, A. G. Plasmonics for future biosensors. *Nat. Photon.* **6**, 709–713 (2012).
- Mubeen, S., Lee, J., Singh, N., Krämer, S., Stucky, G. D. & Moskovits, M. An autonomous photosynthetic device in which all charge carriers derive from surface plasmons. *Nat. Nanotech.* **8**, 247–251 (2013).
- Hu, M. S., Chen, H. L., Shen, C. H., Hong, L. S., Huang, B. R., Chen, K. H. & Chen, L. C. Photosensitive gold-nanoparticle-embedded dielectric nanowires. *Nat. Mater.* **5**, 102–106 (2006).
- Lu, Y. J., Kim, J., Chen, H. Y., Wu, C., Dabidian, N., Sanders, C. E., Wang, C. Y., Lu, M. Y., Li, B. H., Qiu, X., Chang, W. H., Chen, L. J., Shvets, G., Shih, C. K. & Gwo, S. Plasmonic nanolaser using epitaxially grown silver film. *Science* **337**, 450–453 (2012).
- Schuller, J. A., Barnard, E. S., Cai, W., Jun, Y. C., White, J. S. & Brongersma, M. L. Plasmonics for extreme light concentration and manipulation. *Nat. Mater.* **9**, 193–204 (2010).
- Garcia-Vidal, F. J. & Pendry, J. B. Collective theory for surface enhanced Raman scattering. *Phys. Rev. Lett.* **77**, 1163–1166 (1996).
- Roy, P. K., Huang, Y. F. & Chattopadhyay, S. Detection of melamine on fractals of unmodified gold nanoparticles by surface-enhanced Raman scattering. *J. Biomed. Optics* **19**, 011002–011011 (2014).
- Cao, L., White, J. S., Park, J. S., Schuller, J. A., Clemens, B. M. & Brongersma, M. L. Engineering light absorption in semiconductor nanowire devices. *Nat. Mater.* **8**, 643–647 (2009).
- Chattopadhyay, S., Chen, L. C. & Chen, K. H. Energy production and conversion applications of one-dimensional semiconductor nanostructures. *NPG Asia Mater.* **3**, 74–81 (2011).
- Chattopadhyay, S., Lo, H. C., Hsu, C. H., Chen, L. C. & Chen, K. H. Surface-enhanced Raman spectroscopy using self-assembled silver nanoparticles on silicon nanotips. *Chem. Mater.* **17**, 553–559 (2005).
- Dawson, P., Duenas, J. A., Boyle, M. G., Doherty, M. D., Bell, S. E. J., Kern, A. M., Martin, O. J. F., Teh, A.-S., Teo, K. B. K. & Milne, W. I. Combined antenna and localized plasmon resonance in Raman scattering from random arrays of silver-coated, vertically aligned multiwalled carbon nanotubes. *Nano Lett.* **11**, 365–371 (2011).
- Oh, Y. J. & Jeong, K. H. Glass nanopillar arrays with nanogap-rich silver nanoinlands for highly intense surface enhanced Raman scattering. *Adv. Mater.* **24**, 2234–2237 (2012).
- Tang, H. B., Tang, H., Meng, G., Huang, Q., Zhang, Z., Huang, Z. & Zhu, C. Arrays of cone-shaped ZnO nanorods decorated with Ag nanoparticles as 3D surface-enhanced Raman scattering substrates for rapid detection of trace polychlorinated biphenyls. *Adv. Funct. Mater.* **22**, 218–224 (2012).
- Li, X. H., Chen, G. Y., Yang, L. B., Jin, Z. & Liu, J. H. Multifunctional Au-coated TiO₂ nanotube arrays as recyclable SERS substrates for multifold organic pollutants detection. *Adv. Funct. Mater.* **20**, 2815–2824 (2010).
- Chen, Y., Cruz-Chu, E. R., Woodard, J. C., Gartia, M. R., Schulten, K. & Liu, L. Electrically induced conformational change of peptides on metallic nanosurfaces. *ACS Nano* **6**, 8847–8856 (2012).
- Angelis, F. D., Gentile, F., Mecarini, F., Das, G., Moretti, M., Candeloro, P., Coluccio, M. L., Cojoc, G., Accardo, A., Liberale, C., Zaccaria, R. P., Perozziello, G., Tirinato, L., Toma, A., Cuda, G., Cingolani, R. & Fabrizio, E. D. Breaking the diffusion limit with super-hydrophobic delivery of molecules to plasmonic nanofocusing SERS structures. *Nat. Photon.* **5**, 682–687 (2011).
- Angelis, F. D., Malerba, M., Patrini, M., Miele, E., Das, G., Toma, A., Proietti Zaccaria, R. & Fabrizio, E. D. 3D hollow nanostructures as building blocks for multifunctional plasmonics. *Nano Lett.* **13**, 3553–3558 (2013).

- 19 Tian, B., Liu, J., Dvir, T., Jin, L., Tsui, J. H., Qing, Q., Suo, Z., Langer, R., Kohane, D. S. & Lieber, C. M. Macroporous nanowire nanoelectronic scaffolds for synthetic tissues. *Nat. Mater.* **11**, 986–994 (2012).
- 20 Li, J. F., Li, J. F., Huang, Y. F., Ding, Y., Yang, Z. L., Li, S. B., Zhou, X. S., Fan, F. R., Zhang, W., Zhou, Z. Y., Wu, D. Y., Ren, B., Wang, Z. L. & Tian, Z. Q. Shell-isolated nanoparticle-enhanced Raman spectroscopy. *Nature* **464**, 392–395 (2010).
- 21 Liu, T. Y., Tsai, K. T., Wang, H. H., Chen, Y., Chen, Y. H., Chao, Y. C., Chang, H. H., Lin, C. H., Wang, J. K. & Wang, Y. L. Functionalized arrays of Raman-enhancing nanoparticles for capture and culture-free analysis of bacteria in human blood. *Nat. Commun.* **2**, 538–538 (2011).
- 22 Moskovits, M. Surface-enhanced spectroscopy. *Rev. Mod. Phys.* **57**, 783–826 (1985).
- 23 Nie, S. M. & Emery, S. R. Probing single molecules and single nanoparticles by surface-enhanced Raman scattering. *Science* **275**, 1102–1106 (1997).
- 24 Li, M., Gou, H. L., Al-Ogaidi, I. & Wu, N. Q. Nanostructured sensors for detection of heavy metals: a review. *ACS Sustain. Chem. Eng.* **1**, 713–723 (2013).
- 25 Aragay, G., Pino, F. & Merkoçi, A. Nanomaterials for sensing and destroying pesticides. *Chem. Rev.* **112**, 5317–5338 (2012).
- 26 Hsu, C. H., Lo, H. C., Chen, C. F., Wu, C. T., Hwang, J. S., Das, D., Tsai, J., Chen, L. C. & Chen, K. H. Generally applicable self-masked dry etching technique for nanotip array fabrication. *Nano Lett.* **4**, 471–475 (2004).
- 27 Hsu, C. H., Huang, Y. F., Chen, L. C., Chattopadhyay, S., Chen, K. H., Lo, H. C. & Chen, C. F. Morphology control of silicon nanotips fabricated by electron cyclotron resonance plasma etching. *J. Vac. Sci. Technol. B* **24**, 308–311 (2006).
- 28 Huang, Y. F., Chattopadhyay, S., Jen, Y. J., Peng, C. Y., Liu, T. A., Hsu, Y. K., Pan, C. L., Lo, H. C., Hsu, C. H., Chang, Y. H., Lee, C. S., Chen, K. H. & Chen, L. C. Improved broadband and quasi-omnidirectional anti-reflection properties with biomimetic silicon nanostructures. *Nat. Nanotechnol.* **2**, 770–774 (2007).
- 29 Edward, D. in *Handbook of Optical Constants of Solids* (ed. Palik, E.) (Academic Press, New York, 1985).
- 30 Huang, Y. F. & Chattopadhyay, S. Nanostructure surface design for broadband and angle-independent antireflection. *J. Nanophoton.* **7**, 073594–073598 (2012).
- 31 Wang, B. M. & Leu, P. W. Tunable and selective resonant absorption in vertical nanowires. *Opt. Lett.* **37**, 3756–3758 (2012).
- 32 Srivastava, S., Sinha, R. & Roy, D. Toxicological effects of malachite green. *Aquat. Toxicol.* **66**, 319–329 (2004).
- 33 Mondo, K., Hammerschlag, N., Basile, M., Pablo, J., Banack, S. A. & Mash, D. C. Cyanobacterial neurotoxin β -N-methylamino-L-alanine (BMAA) in sark fins. *Mar. Drugs* **10**, 509–520 (2012).
- 34 He, L. L., Kim, N. J., Li, H., Hu, Z. & Lin, M. Use of a fractal-like gold nanostructure in surface-enhanced Raman spectroscopy for detection of selected food contaminants. *J. Agric. Food Chem.* **56**, 9843–9847 (2008).
- 35 Huang, J. A., Zhao, Y. Q., Zhang, X. J., He, L. F., Wong, T. L., Chui, Y. S., Zhang, W. J. & Lee, S. T. Ordered Ag/Si nanowires array: wide-range surface-enhanced Raman spectroscopy for reproducible biomolecule detection. *Nano Lett.* **13**, 5039–5045 (2013).
- 36 Sun, Y. H., Liu, K., Miao, J., Wang, Z., Tian, B., Zhang, L., Li, Q., Fan, S. & Jiang, K. Highly sensitive surface-enhanced Raman scattering substrate made from superaligned carbon nanotubes. *Nano Lett.* **10**, 1747–1753 (2010).
- 37 Altun, A. O., Youn, S. K., Yazdani, N., Bond, T. & Park, H. G. Metal-dielectric-CNT nanowires for femtomolar chemical detection by surface enhanced Raman spectroscopy. *Adv. Mater.* **25**, 4431–4436 (2013).
- 38 Schierhorn, M., Lee, S. J., Boettcher, S. W., Stucky, G. D. & Moskovits, M. Detection of melamine on fractals of unmodified gold nanoparticles by surface-enhanced Raman scattering. *Adv. Mater.* **18**, 2829–2832 (2006).
- 39 Stockman, M. I. Nanoplasmonics: past, present, and glimpse into future. *Opt. Express* **19**, 22029–22106 (2011).
- 40 Bohren, C. F. & Huffman, D. R. *Absorption and Scattering of Light by Small Particles*, Chapter 12 (Wiley, New York, 1983).
- 41 Kelly, K. L., Coronado, E., Zhao, L. L. & Schatz, G. C. The optical properties of metal nanoparticles: the influence of size, shape, and dielectric environment. *J. Phys. Chem. B* **107**, 668–677 (2003).
- 42 Chen, H. J., Shao, L., Ming, T., Woo, K. C., Man, Y. C., Wang, J. F. & Lin, H. Q. Observation of the Fano resonance in gold nanorods supported on high-dielectric-constant substrates. *ACS Nano* **5**, 6754–6763 (2011).
- 43 Kim, A., Ou, F. S., Ohlberg, D. A. A., Hu, M., Williams, R. S. & Li, Z. Study of molecular trapping inside gold nanofinger arrays on surface-enhanced Raman substrates. *J. Am. Chem. Soc.* **133**, 8234–8239 (2011).
- 44 Chu, Y. H., Banaee, M. G. & Crozier, K. B. Double-resonance plasmon substrates for surface-enhanced Raman scattering with enhancement at excitation and Stokes frequencies. *ACS Nano* **4**, 2804–2810 (2010).
- 45 Wei, W. B., Chen, K. & Ge, G. L. Strongly coupled nanorod vertical arrays for plasmonic sensing. *Adv. Mater.* **25**, 3863–3868 (2013).
- 46 Doherty, M. D., Murphy, A., Pollard, R. J. & Dawson, P. Surface-enhanced Raman scattering from metallic nanostructures: bridging the gap between the near-field and far-field responses. *Phys. Rev. X* **3**, 011001–011012 (2013).
- 47 Kabashin, A. V., Evans, P., Pastkovsky, S., Hendren, W., Wurtz, G. A., Atkinson, R., Pollard, R., Podolskiy, V. A. & Zayats, A. V. Plasmonic nanorod metamaterials for biosensing. *Nat. Mater.* **8**, 867–871 (2009).
- 48 Esteban, R., Borisov, A. G., Nordlander, P. & Aizpurua, J. Bridging quantum and classical plasmonics with a quantum-corrected model. *Nat. Commun.* **3**, 825–829 (2012).
- 49 Wang, X. T., Shi, W. S., She, G. W. & Mu, L. X. Surface-enhanced Raman scattering (SERS) on transition metal and semiconductor nanostructures. *Phys. Chem. Chem. Phys.* **14**, 5891–5901 (2012).



This work is licensed under a Creative Commons Attribution-NonCommercial-NoDerivs 3.0 Unported License. The images or other third party material in this article are included in the article's Creative Commons license, unless indicated otherwise in the credit line; if the material is not included under the Creative Commons license, users will need to obtain permission from the license holder to reproduce the material. To view a copy of this license, visit <http://creativecommons.org/licenses/by-nc-nd/3.0/>

Supplementary Information accompanies the paper on the NPG Asia Materials website (<http://www.nature.com/am>)